university of groningen / faculty of science and engineering

Dipole Source Localization using the Continuous Wavelet Transform Method in a Dynamic Fluid Simulation

Bachelor's Project Thesis

Ingeborg van Keulen, i.van.keulen.1@student.rug.nl,
Supervisors: Dr S.M. van Netten & B. J. Wolf

Abstract: There are different methods available to localize a vibrating source in water using Artificial Lateral Lines that measure velocity profiles. There are several methods to reconstruct the location from a velocity profile. One of these methods is the continuous wavelet transform (CWT). The CWT method is a template matching method, which uses wavelets as templates. The CWT method has been tested on dipoles producing potential flow, which describes an ideal fluid. A more realistic fluid may have turbulence or vorticity, which is caused by viscosity. In this research, the performance of the CWT method has been evaluated on different fluid flow models: non-viscous potential flow (with and without added noise), simulated laminar flow and simulated turbulent flow. The results show that the CWT method is resilient to noise up to a moderate degree. The performance of the CWT method in simulated laminar and turbulent flow does not decrease much with respect to potential flow, although the error landscape becomes slightly more complex. The performance of the CWT is a promising method for source localization applications with data in the real world.

1 Introduction

Due to the lack of light deep into the ocean it is hard to, for instance, find crashed airplanes, navigating submarines or doing research on fish. Being able to localize objects in the underwater world would make these things easier to do. Fish already have such a system of sensing organs, which is referred to as the lateral line. The lateral line is "a highly refined sensory system for the detection of water movements, pressure fluctuations or both" (Bleckmann and Zelick, 2009). Fish use this system to identify the direction of an object (Knight, 2011) and the location of an object (Dijkgraaf, 1963).
In (Ćurčić-Blake and Van Netten, 2006), they have found that information on the location and vibration angle of a vibrating source can be extracted from the excitation pattern of pressure gradients. The researchers have compared excitation patterns along the lateral line to theoretical predictions of the location, which were in good agreement. The researchers have also introduced a promising algorithm which can potentially be used to localize a source and its axis of vibrations. This algorithm is referred to as the continuous wavelet transform (CWT). The continuous wavelet transform is a template matching method used to localize a source.
The CWT method has been tested elsewhere (Ćurčić-Blake and Van Netten, 2006) on an idealistic situation, but it would be more interesting to know its performance on a more realistic situation. In this study, the goal is to get a better view of the performance of the CWT method proposed in (Ćurčić-Blake and Van Netten, 2006). For this reason, the CWT method will be used to localize a source in different fluid flows. The fluid flows that will be used are potential flow, potential flow with added noise, laminar flow and turbulent flow. The predicted locations are compared with the real locations and their distances are the localization errors. The errors between different sources in each flow and the errors between different flows will be compared. These comparisons give us more information on the potential use of the CWT method.

2 Background

2.1 Fluid Flows

Potential flow is a flow model of an ideal fluid, which is the flow a fluid undergoes ideally. For a fluid to be an ideal fluid, it should have the properties that it is incompressible and that its flow is irrotational. A fluid is incompressible if its density is constant and a flow is irrotational if the flow has no turbulence. Vorticity is used to describe whether a flow is rotational; no vorticity causes an irrotational flow. Vorticity is dependent of viscosity, which is a fluid characteristic to describe the thickness of a fluid. If there is no viscosity, thus viscosity is zero, then there cannot be vorticity.
The potential flow model is the simplest fluid flow model, however it is also unrealistic because of the lack of turbulence. "Most flows occurring in nature and in engineering applications are turbulent" (Tennekes and Lumley, 1972), hence a more realistic flow model has some turbulence. Therefore a realistic flow model has a flow in which the viscosity and vorticity are set to non-zero.
Depending on the level of turbulence the flow can either be a laminar flow or a turbulent flow, with the difference that a turbulent flow is more chaotic. Reynolds number is used to predict if a flow is laminar or turbulent. A low Reynolds number corresponds with laminar flow and a high Reynolds number with turbulent flow. Reynolds number is defined in equation 2.1, where ρ ($\frac{\text{kg}}{\text{m}^3}$) is the density of the fluid, v ($\frac{\text{m}}{\text{s}}$) is the velocity of the flow, L (m) is the length scale of flow and μ ($\frac{\text{kg}}{\text{ms}}$) is the dynamic viscosity of the fluid.

$$Re = \frac{\rho v L}{\mu} \tag{2.1}$$

In contrast to classical definitions, laminar flow is defined here as a fluid flow model in which vorticity is restricted. Turbulent flow is defined as a fluid flow model in which vorticity is enabled.

2.2 Velocity Profiles

The performance of the continuous wavelet transform can be measured in localization errors. In order to test the performance of the CWT on sources in different fluid flows, velocity profiles were needed. A velocity profile is a figure that shows the velocity of a fluid flow as a function of distance. The velocity profiles are a result of the vibration of a source in a fluid.

2.3 Continuous Wavelet Transform

The continuous wavelet transform is a template matching method used to localize a source. The CWT is similar to the Fourier transform, which decomposes a waveform into sines and cosines. A waveform is a function of some variable, for example time. The difference between the CWT and Fourier transform is that in wavelet analysis, the sines and cosines are replaced with wavelet functions or wavelets. "Wavelets are mathematical functions that cut up data into different frequency components, and then study each component with a resolution matched to its scale." (Graps, 1995). In equations 2.2 and 2.3, two wavelets are defined which are referred to as the even and odd wavelet, respectively (Ćurčić-Blake and Van Netten, 2006). Both wavelets meet the admissibility condition. The admissibility condition requires a wavelet to have zero mean and it must be scalable both in amplitude and in width.
In these equations, the parameter s corresponds to the sensor position with respect to an initially chosen reference sensor position, b corresponds to the position of the source along the sensors and d corresponds to the distance to the sensors, as shown in Figure 3.1.
In the case that the sensors are sensitive in the direction along the sensor array, then the v_x velocity profile can be defined as equation 2.4. In this equation W corresponds with the speed of the source, a with the radius of the source and d with the distance to the sensor array. The vibration angle φ denotes the direction a source is moving to. The vibration angle was measured counter-clockwise from the origin, as shown in Figure 3.1.
In equations 2.5 and 2.6, a convolution-like multiplication operation of the velocity profile with the wavelets along the sensor array is performed. A two-dimensional energy plot can be obtained from equation 2.8, in which the maximum value is an approximation of the real location of the source. This equation is a combination of equations 2.5, 2.6 and 2.7.

$$\psi_e(s,b,d) = \frac{1 - 2\left(\frac{s-b}{d}\right)^2}{\left[1 + \left(\frac{s-b}{d}\right)^2\right]^{\frac{5}{2}}} \tag{2.2}$$

$$\psi_o(s,b,d) = \frac{-3\left(\frac{s-b}{d}\right)}{\left[1 + \left(\frac{s-b}{d}\right)^2\right]^{\frac{5}{2}}} \tag{2.3}$$

$$v_x = \frac{Wa^3}{2d^3}\psi_e \cos(\varphi) + \psi_o \sin(\varphi) \tag{2.4}$$

$$F_e(b,d) = \frac{1}{\sqrt{d}} \int_{-\infty}^{\infty} f(s) \cdot \psi_e(s,b,d) ds \tag{2.5}$$

$$F_o(b,d) = \frac{1}{\sqrt{d}} \int_{-\infty}^{\infty} f(s) \cdot \psi_o(s,b,d) ds \tag{2.6}$$

$$c_1 = \frac{c_{odd}}{c_{even}} = \frac{5}{3} \tag{2.7}$$

$$F_{com,eo}(b,d) = \sqrt{c_1 F_e^2(b,d) + F_o^2(b,d)} \tag{2.8}$$

In the case that the sensors are sensitive in the direction perpendicular to the sensor array, then the v_y velocity profile can be defined as equation 2.10. This equation uses equation 2.9, which is referred to as a navelet (NotAwaVELET). The navelet has not zero mean and is therefore not a wavelet, but is known as a non-zero integral.

$$\psi_n(s,b,d) = \frac{2 - \left(\frac{s-b}{d}\right)^2}{\left[1 + \left(\frac{s-b}{d}\right)^2\right]^{\frac{5}{2}}} \tag{2.9}$$

$$v_y = \frac{Wa^3}{2d^3}\psi_o \cos(\varphi) + \psi_n \sin(\varphi) \tag{2.10}$$

The location of a source using the v_y profile can be obtained in the same way as with a v_x profile, but using equation 2.13 instead of equation 2.8. Equation 2.13 uses equations 2.6, 2.11 and 2.12 (Bot, 2019) to localize a source.

$$F_n(b,d) = \frac{1}{\sqrt{d}} \int_{-\infty}^{\infty} f(s) \cdot \psi_n(s,b,d) ds \tag{2.11}$$

$$c_2 = \frac{c_{odd}}{c_{nav}} = \frac{15}{41} \tag{2.12}$$

$$F_{com,on}(b,d) = \sqrt{c_2 F_n^2(b,d) + F_o^2(b,d)} \tag{2.13}$$

3 Methods

3.1 Data Generation

The performance of the CWT can be measured in localization errors. In order to test the performance of the CWT on sources in different fluid flows, the corresponding velocity profiles were needed. The profiles for potential flow were obtained with the equations described in section 2.3. The profiles for laminar flow and turbulent flow were obtained using the open-source framework mantaflow (Pfaff and Thuerey, 2018). After having obtained the profiles, they had to be pre-processed before they could be used in the CWT.

3.1.1 Setup

In Figure 3.1 a vibrating source, from now on referred to a a dipole, is depicted as a black dot. The dipole has a vibration angle φ with respect to the sensor array. The dipole is switching its direction every 5 seconds from φ to $\varphi - 180°$, creating a vibration in the fluid. The flow model had a grid with length x and height y and the dipole can be placed on a specific point from the grid. This point is described in terms of b and d (Figure 3.1). The distance in the x-direction from an initially chosen reference point on the sensor array to the dipole is denoted by b. The distance perpendicular from the sensor array to the dipole is denoted by d.

3.1.2 Potential Flow and Noise

The velocity profiles of potential flow can be obtained with equations 2.4 and 2.10 for the horizontal v_x and vertical v_y components of the velocity field, respectively.
To add noise to a velocity profile, a new profile was created with the same length as the velocity profile. Each value was initialized as a random value between -1 and 1 and was then multiplied with a manually chosen constant.

3.1.3 Mantaflow

To generate the velocity profiles for flows using viscosity and thus vorticity, the open-source framework mantaflow was used. Mantaflow is “targeted at fluid simulation research in Computer Graphics” (Pfaff and Thuerey, 2018). In this framework, a flow

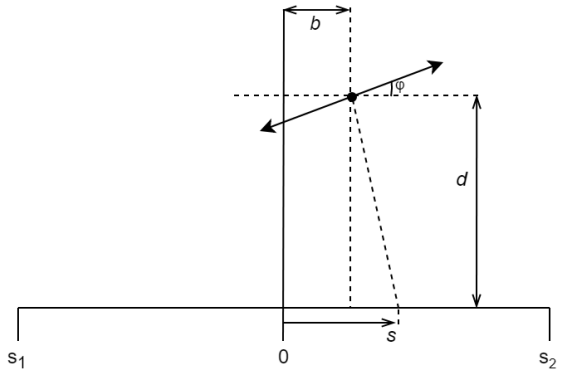

Figure 3.1: A schematic representation of the experimental setup. The horizontal axis represents the sensor array and s denotes the location on the sensor array. A source has a vibration angle φ, with respect to the sensor array. The distance from the sensor array to the source is denoted by d, and the distance along the sensor array with b.

model was built involving a dipole for different settings of viscosity. The used version of mantaflow was version 0.12.
With each flow model, different simulations were performed. Each simulation contained n frames, which represent time steps. In a simulation, the viscosity of the fluid and the speed of the dipole can be changed to simulate no turbulence or some turbulence. The simulation grid, which resembles a velocity field, was stored for each frame.

3.1.4 Example Velocity Profiles

In this research velocity profiles are obtained for both the horizontal v_x and vertical v_y components of velocity. Some examples of (normalized) velocity profiles of potential flow can be seen in Figure 3.2. The velocity profiles of the same sources, but obtained in mantaflow in a laminar flow simulation can be seen in Figure 3.3.

3.2 Experiments

3.2.1 Pre-processing Data

Before the CWT method can be used on the velocity profiles, there were some pre-processing steps that were performed first. In case of the velocity

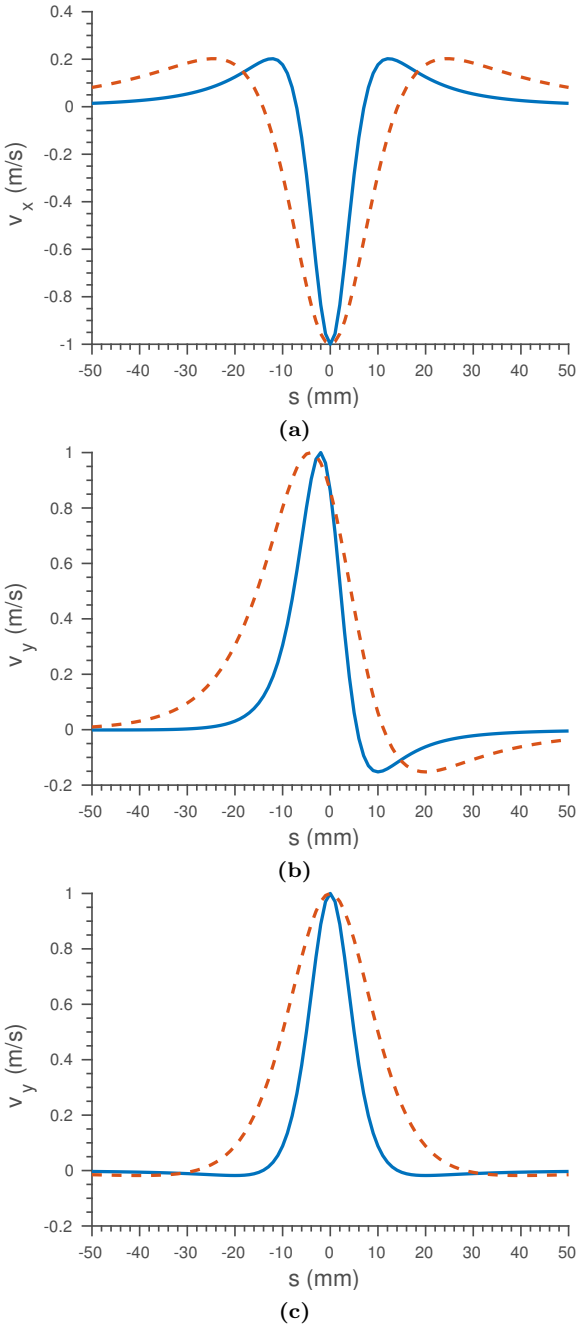

Figure 3.2: Velocity profiles as a function of sensor position along the sensor array (s), obtained with equations 2.4 and 2.10. The source is positioned at b=0 mm, and at two positions of d: 10 mm (solid line) and 20 mm (dashed line). (a) shows $v_{x,pot}$ with φ=0°, (b) shows $v_{y,pot}$ with φ=45°, (c) shows $v_{y,pot}$ with φ=90°.

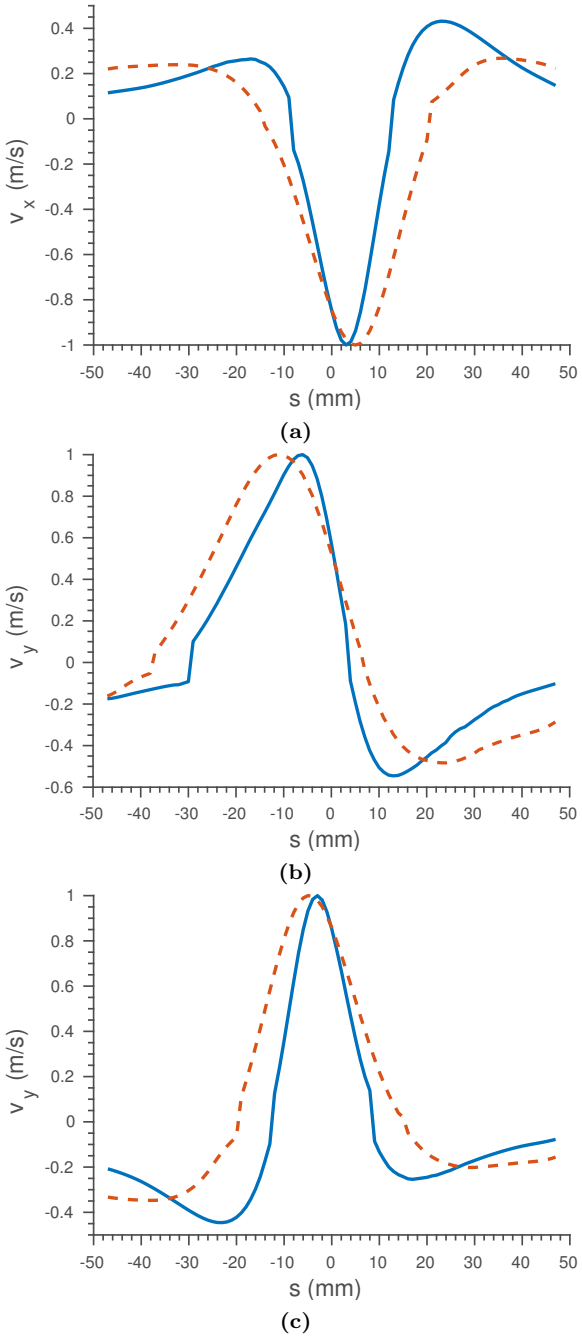

Figure 3.3: Velocity profiles as a function of sensor position along the sensor array (s), obtained with mantaflow in a laminar flow simulation. The source is positioned at b=0 mm, and at two positions of d: 10 mm (solid line) and 20 mm (dashed line). (a) shows $v_{x,lam}$ with φ=0°, (b) shows $v_{y,lam}$ with φ=45°, (c) shows $v_{y,lam}$ with φ=90°.

profiles for potential flow, they should be normalized. In order to do this, all the values of a profile were divided by the maximum value of that profile. In case of the velocity profiles obtained in mantaflow, there were more steps. In each grid, the pixels from the lower, horizontal part represented the sensor locations. These sensors all measured a part of the velocity field, which consisted of two components; the velocity in the x-direction and the velocity in the y-direction. In each simulation, these measurements were taken for all the frames. The next step involved dividing all the measurements by the absolute maximum of the measurements in order to only have values between -1 and 1. After having rescaled the measurements, the absolute maximum value for each sensor over all frames (aka time steps) was taken to get one (normalized) velocity profile for each velocity component.

3.2.2 Parameter Settings

To do all the experiments with laminar flow and turbulent flow, there were in total 18854 simulations performed in mantaflow. Each simulation was performed in the same grid, which had a width of 100 grid cells and a height of 50 grid cells. The dipole had a radius of 5 grid cells.
For each simulation, 250 frames were used. For each frame, 95 sensors were selected from the 5th row from the bottom. On each grid cell, a sensor was placed, except for the first and last three grid cells. In each simulation, the dipole was put on a different grid cell and/or was vibrating in a different direction. After all the simulations were performed, all source locations were used to compare the performance of the CWT method for different fluid flows. All together there were 5151 locations with two angles in the experiments with potential flow (with and without noise) and 4646 location with two angles in the the experiments with simulated data.

3.2.3 Evaluation

To evaluate the performance of the CWT, the euclidean distance (ED) between the predicted location and the real location of the dipole was used as an error measure. The euclidean distance was calculated using equation 3.1. In this equation p corresponds to the predicted location, where p_x

and p_y refer to the predicted x-coordinate and y-coordinate. In this equation r corresponds to the real location of the dipole.

$$d(p, r) = \sqrt{(r_x - p_x)^2 + (r_y - p_y)^2} \tag{3.1}$$

3.2.4 Comparisons

To visualize the dependence of localization errors on the location of the dipole itself, heat maps were used. Heat maps give a better idea of areas of grid cells in which dipoles are more difficult to localize with the CWT method. The heat map limits are set to 0 as minimum and 50 as maximum, to make the visual comparison between different heat maps easier. For each fluid flow model, the localization errors are expected to increase if d is increasing and/or to slightly increase if b is getting more distant to the center of the sensor array. To visualize the difference in localization errors between different fluid flows, histograms were used.
A comparison will be made between the localization errors for potential flow with and without added noise. This comparison should show the influence of noise on the CWT localization errors. The localization errors for potential flow with noise are expected to have an overall increase in contrast to potential flow without noise, with the largest increase in locations with the greatest distance d to the sensor array.
Another comparison will be made between the localization errors for laminar flow and turbulent flow. The localization errors of turbulent flow are expected to be overall larger in comparison with the localization errors of laminar flow. In both comparisons, the reason for the expectations are the same. Potential flow with added noise and turbulent flow are both more chaotic and irregular in contrast to potential flow without added noise and laminar flow. These irregularities cause the CWT method to make larger errors.

4 Results

In this research, the sensors can only measure the velocity field of a dipole located at a positive distance with respect to the sensor array. In mantaflow the dipole has a radius of 5 mm, which implies that if $d < 5$ mm, then the dipole is moving "through" the sensor array. Therefore the source is placed only on grid cells with a distance $d \geq 5$ mm.

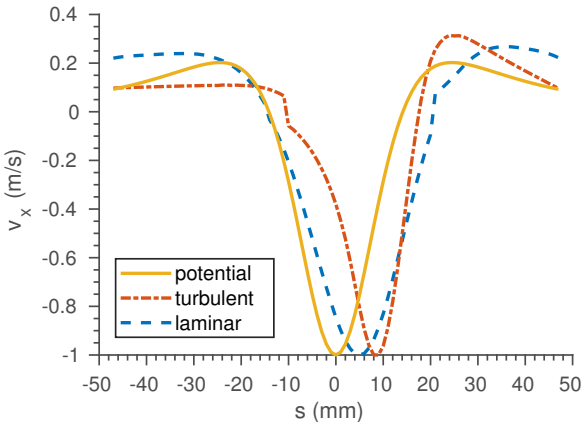

Figure 4.1: The v_x profiles for a dipole placed at (0, 20), vibrating with φ=0°. The profile for potential flow is obtained with equation 2.4 and the mantaflow profiles are obtained with mantaflow in a laminar flow simulation and in a turbulent flow simulation.

4.1 Data Generation

4.1.1 Peak Shift

Figure 4.1 shows the velocity profiles for a dipole with φ=0° placed at (0, 20), in different fluid flows. The profile for potential flow is obtained with equation 2.4. The profile for laminar flow is expected to resemble the potential flow profile. The profiles obtained with mantaflow have their peaks shifted to the right of the expected profile. The profile for laminar flow has its peak 5 grid cells to the right of the peak of the expected profile and the profile for turbulent flow 9 grid cells. Most dipoles placed on other grid cells also show a shift between the expected peak and real peak, however the amount of shift was too irregular to make any corrections.

4.1.2 Velocity Profiles

Figure 4.2 and Figure 4.3 show velocity profiles for a dipole placed in different fluid flows, on different locations. The shape of the laminar flow profiles resembles the shape of the potential flow profiles, but it does not follow the potential flow profile exactly.

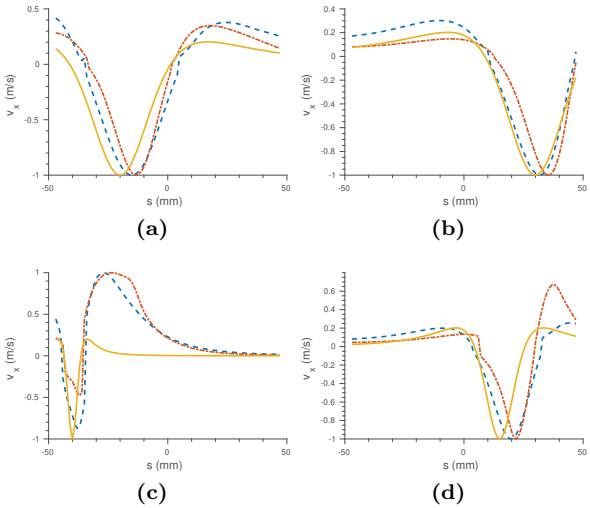

Figure 4.2: The v_x velocity profiles for three different fluid flows: potential flow (solid line), laminar flow (dashed line) and turbulent flow (dash-dotted line). The velocity profiles are shown for a dipole with $\varphi = 0°$, positioned at different locations. (a) shows the dipole positioned at b=-20 mm and d=30 mm, (b) shows the dipole positioned at b=30 mm and d=30 mm, (c) shows the dipole positioned at b=-40 mm and d=5 mm, (d) shows the dipole positioned at b=15 mm and d=15 mm.

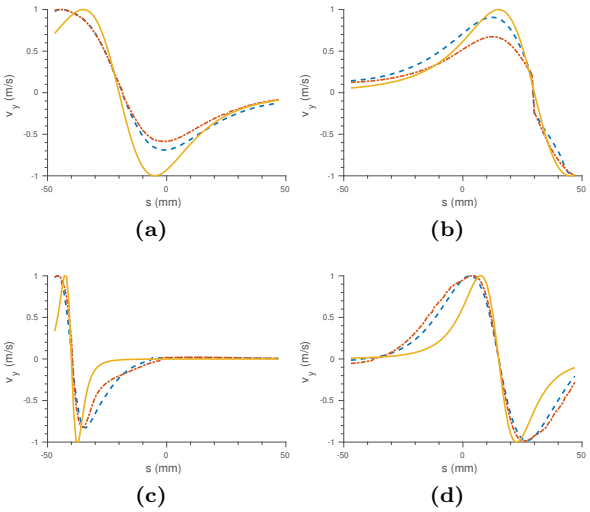

Figure 4.3: The v_y velocity profiles for three different fluid flows: potential flow (solid line), laminar flow (dashed line) and turbulent flow (dash-dotted line). The velocity profiles are shown for a dipole with $\varphi = 0°$, positioned at different locations. (a) shows the dipole positioned at b=-20 mm and d=30 mm, (b) shows the dipole positioned at b=30 mm and d=30 mm, (c) shows the dipole positioned at b=-40 mm and d=5 mm, (d) shows the dipole positioned at b=15 mm and d=15 mm.

The resemblance is better with the v_x profiles in contrast to the v_y profiles. The turbulent velocity profile seems to be only mildly deviating from the laminar velocity profile.'

4.2 Potential Flow (With and Without Added Noise)

4.2.1 Influence Noise

Figure 4.4 shows the influence of adding noise to a (not normalized) velocity profile. An increase in noise magnitude results in larger $\text{CWT}_{x,pot}$ and $\text{CWT}_{y,pot}$ localization errors. In comparison with the other $\text{CWT}_{x,pot}$ and $\text{CWT}_{y,pot}$ localization errors, the $\text{CWT}_{y,pot}$ for a dipole with $\varphi = 90°$ is less affected by noise.

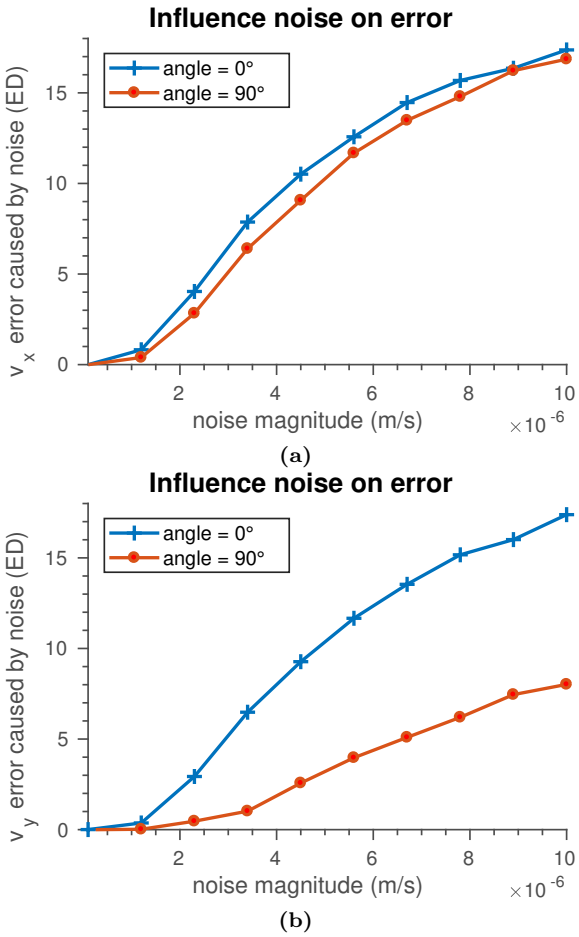

Figure 4.4: The influence of adding different noise magnitudes to: (a) $v_{x,pot}$ velocity profile on the CWT$_{x,pot}$ localization errors, (b) $v_{y,pot}$ velocity profile on the CWT$_{y,pot}$ localization errors.

4.2.2 comparison (heat maps)

Figure 4.5 shows the CWT$_{x,pot}$ localization errors for each (b, d) combination in the form of a heat map. The maximum value of the heat map is set to 50 mm, thus every combination that had a bigger error has the same color that corresponds with an error of 50 mm.
In Figure 4.5, the CWT$_{x,pot}$ localization errors are shown for a dipole with $\varphi = 0°$ for two conditions. The two conditions are 'without noise added' and 'with noise added'. The CWT$_{x,pot}$ localization errors become much larger for $d > 35$ mm in the noise added condition in comparison with the no noise condition. Another difference is that in the no noise condition, the center of the grid has small localization errors, where in the noise added condition this area of smaller errors disappears.

In Figure 4.6, the CWT$_{y,pot}$ localization errors are shown for a dipole with $\varphi = 0°$ for two conditions. The two conditions are 'without noise added' and 'with noise added'. The CWT$_{y,pot}$ localization errors become slightly bigger for $d > 35$ mm in the noise added condition in comparison with the no noise condition.

When comparing Figure 4.5 and Figure 4.6, there are some differences in the error distributions in both conditions. In the no noise condition, the CWT$_{x,pot}$ method has overall smaller localization errors than the CWT$_{y,pot}$ method. Most noticeable are the small CWT$_{x,pot}$ localization errors in the center of the grid, where the CWT$_{y,pot}$ method shows larger localization errors. In the noise condition, the localization errors for $d > 35$ mm become larger for both the CWT$_{x,pot}$ method and the CWT$_{y,pot}$ method. The difference between both methods in the noise added condition is that there are more and larger errors in the CWT$_{x,pot}$ method.

4.2.3 comparison (histograms)

In Figure 4.7, the CWT$_{x,pot}$ localization errors are shown for two conditions for a dipole vibrating with $\varphi = 0°$ and with $\varphi = 90°$. In Figure 4.7 (a), the CWT$_{x,pot}$ localization errors are shown for the condition no noise and the condition noise added. The maximum error with no noise is 27.5 mm and the mean error is 8.2 mm. In the noise added condition the maximum error is 106 mm and the mean error is 14.5 mm. In Figure 4.7 (b), the CWT$_{x,pot}$ local-

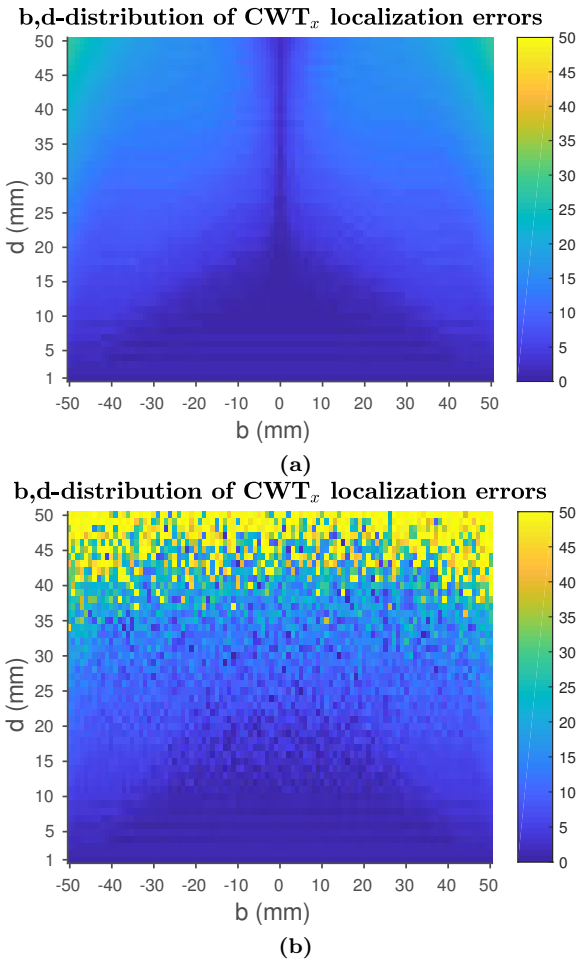

Figure 4.5: Heat maps of the CWT$_{x,pot}$ localization errors for a dipole with $\varphi = 0°$, for two conditions: (a) no noise condition, (b) adding 3e-6 m/s noise condition.

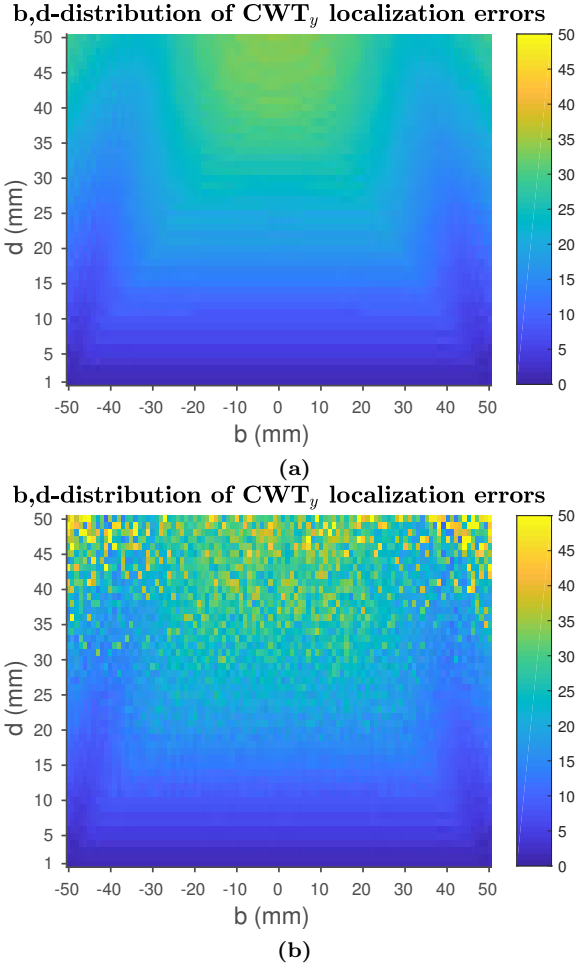

Figure 4.6: Heat maps of the CWT$_{y,pot}$ localization errors for a dipole with $\varphi = 0°$, for two conditions: (a) no noise condition, (b) adding 3e-6 m/s noise condition.

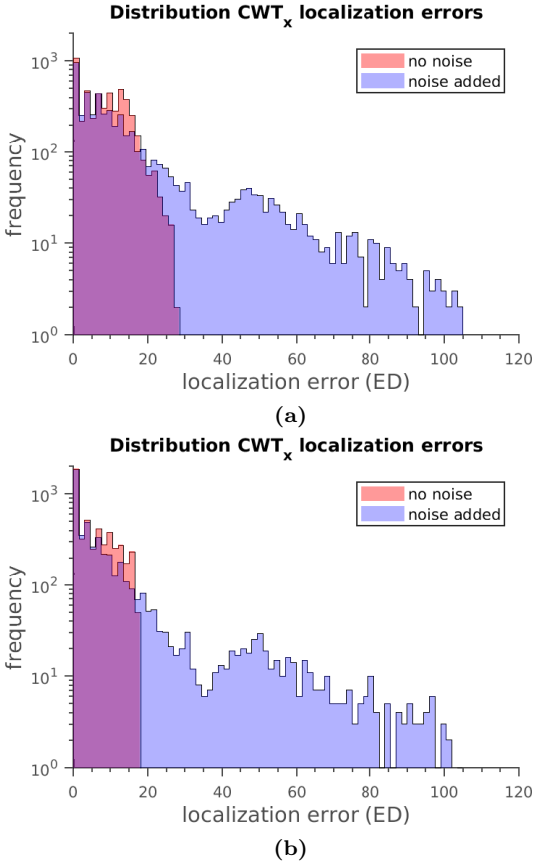

Figure 4.7: Histograms of the CWT$_{x,pot}$ localization errors for two conditions: no noise and 3e-6 m/s noise added. (a) shows CWT$_{x,pot}$ localization errors for a dipole with $\varphi = 0°$, (b) shows CWT$_{x,pot}$ localization errors for a dipole with $\varphi = 90°$.

ization errors are shown for the condition no noise and the condition noise added. The maximum error with no noise is 17.8 mm and the mean error is 5.4 mm. The maximum error with noise added is 107.4 mm and the mean error with noise added is 10.3 mm.
The CWT$_{x,pot}$ localization errors for both a dipole with $\varphi = 0°$ and with $\varphi = 90°$ become larger and are more distributed over a larger range when noise is added. For a dipole with $\varphi = 90°$ the CWT$_{x,pot}$ localization errors are overall smaller in comparison with a dipole with $\varphi = 0°$.

In Figure 4.8, the CWT$_{y,pot}$ localization errors are shown for a dipole vibrating with $\varphi = 0°$ and with $\varphi = 90°$. In Figure 4.8 (a), the CWT$_{y,pot}$ localization errors are shown for the condition no noise and the condition noise added. The maximum error with no noise is 17.1 mm and the mean error is 4.6 mm. In the noise added condition the maximum error is 106.5 mm and the mean error is 9.9 mm. In Figure 4.8 (b), the CWT$_{y,pot}$ localization errors are shown for the condition no noise and the condition noise added. The maximum error with no noise is 348 mm and the mean error is 16.5 mm. The maximum error with noise added is 98.1 mm and the mean error with noise added is 17.4 mm.
The CWT$_{y,pot}$ localization errors for a dipole with $\varphi = 0°$ and with $\varphi = 90°$ are both distributed over a larger range. The difference is that the overall error only increases much for the dipole with $\varphi = 0°$.

When comparing Figure 4.7 and Figure 4.8 for a dipole with $\varphi = 0°$, the differences are small. Overall the CWT$_{y,pot}$ method has smaller errors in comparison with the CWT$_{x,pot}$ method, which results in a smaller mean. There is a big difference between the CWT$_{x,pot}$ and CWT$_{y,pot}$ method for a dipole with $\varphi = 90°$, where the overall error does not increase much when noise is added to the latter.

4.3 Simulated Laminar and Turbulent Flow

4.3.1 Heat Maps

In Figure 4.9, the CWT$_{x,manta}$ localization errors are shown in the form of heat maps. The figure shows the errors for a dipole with $\varphi = 0°$ in two different fluid flow simulations. The two simulations are 'laminar flow' and 'turbulent flow'. Both heat maps show a more dark blue area on the right part of the grid. This area seems to be larger and darker in the laminar flow simulation in contrast to the turbulent flow simulation.

In Figure 4.10, the CWT$_{y,manta}$ localization errors are shown for a dipole with $\varphi = 0°$ in two different fluid flow simulations. The two simulations are 'laminar flow' and 'turbulent flow'. Both simulations show an area on the left part of the grid in which the localization errors are smaller.

When comparing Figure 4.9 and Figure 4.10, there are not many differences. Overall, localizing a dipole with $\varphi = 90°$ results in larger localization errors in contrast to a dipole with $\varphi = 0°$. Another difference is that the CWT$_{x,manta}$ method shows

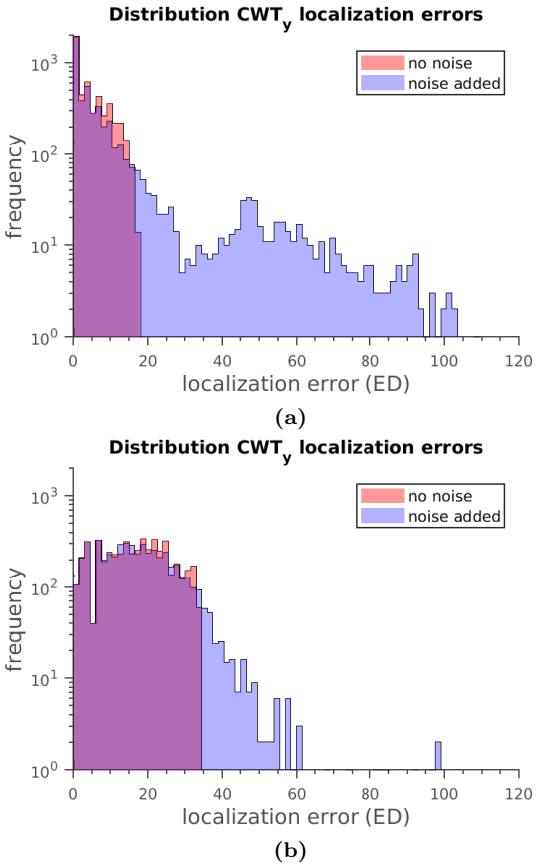

Figure 4.8: Histograms of the CWT$_{y,pot}$ localization errors for two conditions: no noise and 3e-6 m/s noise added. (a) shows CWT$_{y,pot}$ localization errors for a dipole with $\varphi = 0°$, (b) shows CWT$_{y,pot}$ localization errors for a dipole with $\varphi = 90°$.

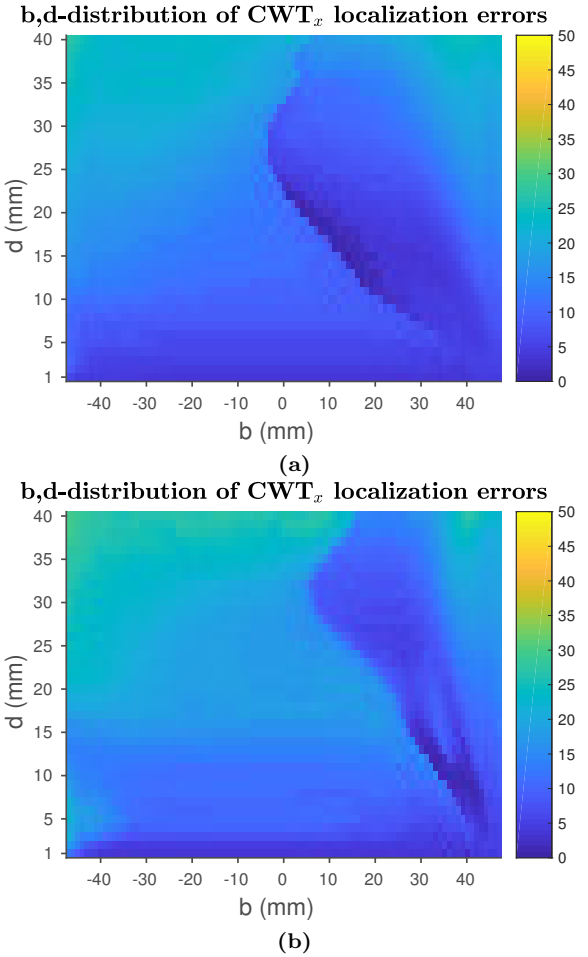

Figure 4.9: Heat maps of the CWT$_{x,manta}$ localization errors for a dipole with $\varphi = 0°$, in two different fluid flow simulations: (a) shows a laminar flow simulation, (b) shows a turbulent flow simulation.

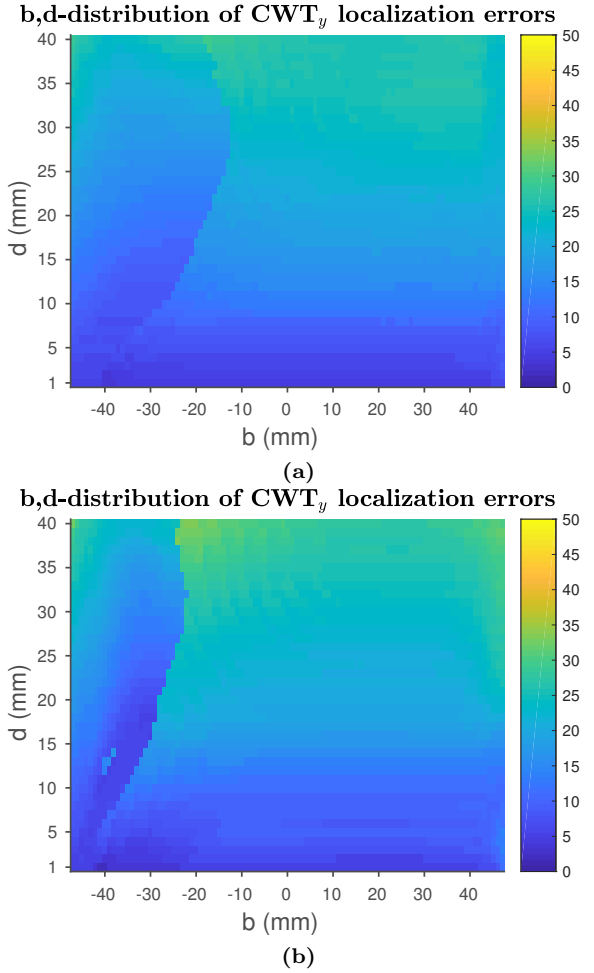

Figure 4.10: Heat maps of the CWT$_{y,manta}$ localization errors for a dipole with $\varphi = 0°$, in two different fluid flow simulations: (a) shows a laminar flow simulation, (b) shows a turbulent flow simulation.

an area with smaller localization errors on the right part of the grid, in contrast to the CWT$_{y,manta}$ method which shows such an area on the left part of the grid. None of the heat maps show localization errors greater than 40 mm.

4.3.2 Histograms

In Figure 4.11, the CWT$_{x,manta}$ localization errors are shown for two simulations for a dipole vibrating with $\varphi = 0°$ and with $\varphi = 90°$. In Figure 4.11 (a), the CWT$_{x,manta}$ localization errors are shown for the simulation laminar flow and turbulent flow. The maximum error with laminar flow is 26.9 mm and the mean error is 12.3 mm. In the turbulent flow the maximum error is 29.8 mm and the mean error is 14.7 mm.
In Figure 4.11 (b), the CWT$_{x,manta}$ localization errors are shown for the simulations laminar flow and turbulent flow. The maximum error with laminar flow is 27.5 mm and the mean error is 5.6 mm. The maximum error with turbulent flow is 27.7 mm and the mean error is 5.8 mm.
When comparing both figures, the biggest difference is that the localization errors for a dipole with $\varphi = 90°$ are smaller in contrast to the errors for a dipole with $\varphi = 0°$. The CWT$_{x,manta}$ localization errors for a dipole with $\varphi = 90°$ show little difference between the two fluid flow simulations. The CWT$_{x,manta}$ localization errors for a dipole with $\varphi = 0°$ are slightly larger in the turbulent flow simulation. Both figures have the errors distributed over a small range.

In Figure 4.12, the CWT$_{y,manta}$ localization errors are shown for two simulations for a dipole vibrating with $\varphi = 0°$ and with $\varphi = 90°$. In Figure 4.12 (a), the CWT$_{y,manta}$ localization errors are shown for the simulation laminar flow and turbulent flow. The maximum error with laminar flow is 29.1 mm and the mean error is 5.7 mm. In the turbulent flow the maximum error is 29.1 mm and the mean error is 5.9 mm. In Figure 4.12 (b), the CWT$_{y,manta}$ localization errors are shown for the simulations laminar flow and turbulent flow. The maximum error with laminar flow is 29.5 mm and the mean error is 16.8 mm. The maximum error with turbulent flow is 33.5 mm and the mean error is 17.4 mm.
When comparing both figures, the biggest difference is that the localization errors for a dipole with

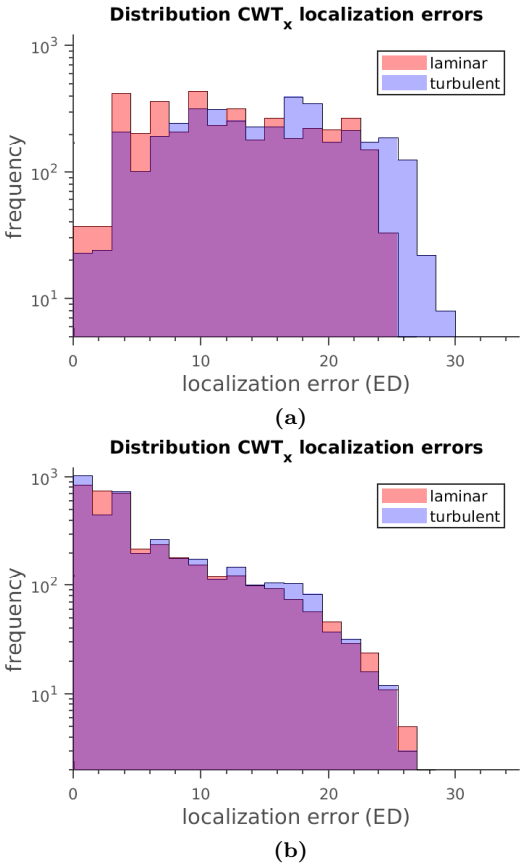

Figure 4.11: Histograms of the CWT$_{x,manta}$ localization errors for a source with two different vibration angles, placed in a laminar flow simulation and in a turbulent flow simulation. (a) shows a dipole with $\varphi = 0°$, (b) shows a dipole with $\varphi = 90°$.

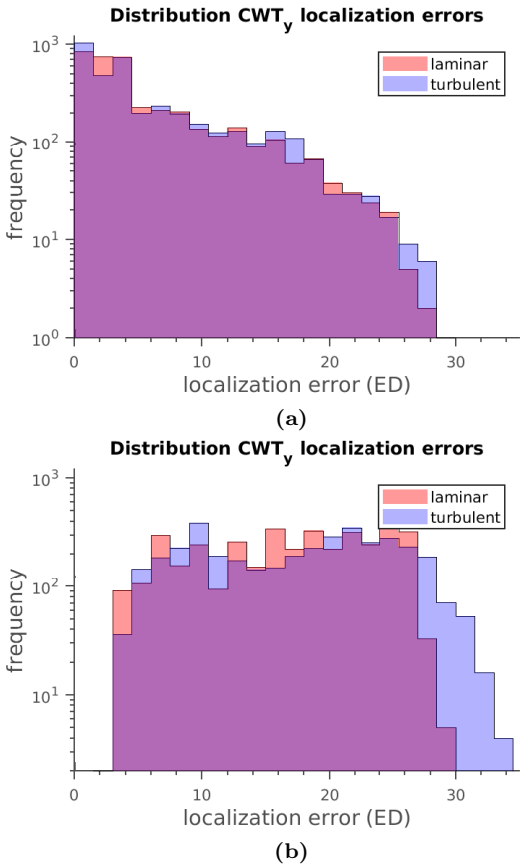

Figure 4.12: Histograms of the CWT$_{y,manta}$ localization errors for a source with two different vibration angles, placed in a laminar flow simulation and in a turbulent flow simulation. (a) shows a dipole with $\varphi = 0°$, (b) shows a dipole with $\varphi = 90°$.

$\varphi = 90°$ are much larger in contrast to the errors for a dipole with $\varphi = 0°$. The CWT$_{x,manta}$ localization errors for a dipole with $\varphi = 0°$ show little difference between the two fluid flow simulations. The CWT$_{x,manta}$ localization errors for a dipole with $\varphi = 90°$ are slightly larger in the turbulent flow simulation. Both figures have the errors distributed over a small range.

The lower figure in Figure 4.11 and the upper figure in Figure 4.12 are similar. The upper figure in Figure 4.11 and the lower figure in Figure 4.12 are slightly similar if the range would have been the same.

5 Discussion

5.1 Interpretation

The results show the CWT localization errors of a dipole positioned in potential flow, potential flow with noise added, a laminar flow simulation and in a turbulent flow simulation. These errors represent the performance of the CWT in the different fluid flows.
The largest range in CWT localization errors is for a dipole positioned in potential flow with noise added. The CWT_x and CWT_y localization errors of this fluid flow model have overall a mean of > 10 mm. The potential flow models were tested in a grid with length 50 mm and width 100 mm. The maximum localization error of a dipole positioned in the center of that grid is 55.9 mm. This implies that the average error in potential flow with noise added, is 17.9% of the maximum possible error.
The mean and maximum CWT localization errors are overall the smallest for a dipole positioned in potential flow. Between a dipole positioned in a laminar flow simulation or in a turbulent flow simulation, the mean and maximum CWT localization errors do not differentiate much. In all different fluid flows, the CWT_x localization errors are the smallest for a dipole with $\varphi = 90°$ and the CWT_y localization errors are the smallest for a dipole with $\varphi = 0°$.
The difference between the performance in a laminar flow and in a turbulent flow simulation is that the localization errors are more unpredictable in a turbulent flow simulation. In both Figure 4.9 and Figure 4.10, it can be seen that the heat maps of a turbulent flow simulation show more abrupt transitions in localization errors. Thus the performance does not decrease when using a turbulent flow simulation instead of a laminar flow simulation, but it does become more unpredictable.

5.2 Improvements

In this research, there were some technical details that may have influenced the results.

5.2.1 Noise Selection

The magnitude of the added noise was chosen manually based on Figure 4.4. Thus it should be noticed that the localization errors in potential flow with noise added depends on the noise magnitude. If having chosen a smaller value for noise magnitude, then the performance of the CWT would have looked different from what it does now.

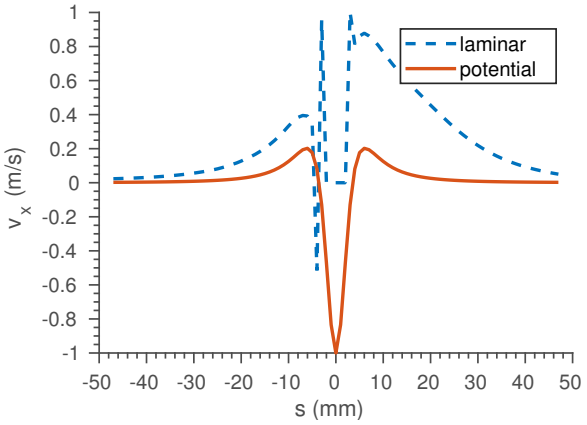

Figure 5.1: The v_x profiles for a dipole vibrating at (0, 5), with φ=0°. The expected profile is obtained with equation 2.4 and the mantaflow profile is obtained with mantaflow in a laminar flow simulation.

5.2.2 Scaling Coefficient

In equation 2.12, the scaling coefficient is determined in (Bot, 2019). This research is still in development, thus the constant might change in the future.

5.2.3 Mantaflow Flaws

The framework mantaflow was used to evaluate the CWT method in a laminar flow simulation and in a turbulent flow simulation. While mantaflow is being actively developed and maintained, the current version still shows some unexpected results which might be the result of a bug. One of these unexpected results can be seen in Figure 5.1. This figure shows a velocity profile obtained with mantaflow, for a dipole positioned at (0, 5) with $\varphi = 0°$. It also shows the expected velocity profile for this dipole, obtained with equation 2.4. For unknown reasons, if a dipole with $\varphi = 0°$ is positioned at a distance $d \leq 10$ mm to the sensor array, then the sensors in mantaflow below the dipole measure only zeros.

The possibility of using flow models with viscosity in mantaflow is a relative new feature. It

was introduced in version 0.11, which was released in July 2017. When comparing the velocity profiles obtained in a laminar flow simulation and in a turbulent flow simulation, the profiles deviate only mildly from each other. See Figure 4.2 and Figure 4.3 for a side by side comparison. It is questionable if this level of turbulence is representative of turbulence in the real world.

6 Conclusion

The continuous wavelet transform method is an algorithm which can be used to localize a source. Currently, this algorithm has been tested in idealistic fluid flows in which there is no viscosity, but not in more realistic fluid flows in which there is viscosity. Evaluating the performance of the CWT in different fluid flows should shed more light on the potential use of the CWT.
The results in this research have shown that the performance of the CWT method for a dipole in potential flow, potential flow with noise added, a laminar flow simulation and in a turbulent flow simulation. The amount of noise added in the potential flow affects the performance of the CWT method significantly. Depending on how the CWT method is desired to be used and therefore what the maximum localization error might be, the amount of noise added can change. If the desire is a method with very small errors, then there cannot be much noise. If the dipole does not have to localized on the exact right location, then more noise is possible. The results also show that the performance of the CWT method decreases only slightly in a more realistic fluid flow model. This is very promising, because the CWT method will most likely be used in applications in the real world. The results also showed that depending on the vibration angle of the dipole, either the CWT_x or the CWT_y method had better approximations of the location.

6.1 Future Research

A possible research might discuss the possibility of combining the CWT_x and CWT_y method. In the current research, the localization errors depended on the chosen method. At this moment, there is not a way of choosing which method to use and therefore a combination of both methods solves the problem of having to choose and might result in lower localization errors.
Another research possibility is a follow-up research in which the greatest uncertainty in this research is solved. The greatest uncertainty is the reliability of the velocity profiles obtained with mantaflow. To be able to tell if the CWT is useful in different fluid flows in the real life world, then it must be certain that the profiles are representative enough of fluid flows in the real world. Therefore a follow-up research could involve obtaining velocity profiles of a dipole placed in laminar flow and in turbulent flow in the real world. This research could then be repeated with these profiles instead of the velocity profiles obtained with mantaflow. The resulting CWT localization errors will give a more reliable measure of its performance, without the discussion whether the input is representative enough of the reality.

References

H. Bleckmann and R. Zelick. Lateral line system of fish. *Integrative Zoology*, 4(1):13–25, 2009.

J. Bot. Master thesis: CWT for dipole localization. *in preparation*, 2019.

B. Ćurčić-Blake and S. M. Van Netten. Source location encoding in the fish lateral line canal. *The Journal of Experimental Biology*, 209(8):1548–1559, 2006.

S. Dijkgraaf. The functioning and significance of the lateral-line organs. *Biological Reviews*, 38(1): 51–105, 1963.

Amara Graps. "An Introduction to Wavelets". *IEEE Comp. Sci. Engi.*, 2:50–61, 02 1995. doi: 10.1109/99.388960.

K. Knight. Lateral line helps fish determine sound direction. *Journal of Experimental Biology*, 214 (20), 2011.

Tobias Pfaff and Nils Thuerey. mantaflow, 2018. URL `http://mantaflow.com/`.

H. Tennekes and J. L. Lumley. *A First Course in Turbulence*. The MIT Press, 1972. ISBN 0-262-20019-8.